AGU PUBLICATIONS

JGR

Journal of Geophysical Research: Atmospheres

RESEARCH ARTICLE
10.1002/2014JD021866

Key Points:
- Multimodal microspectroscopy allows the characterization of individual ice nuclei
- Ice nuclei are not exceptional but represent common particle-type classes in air
- Ice nuclei cloud cycling and surface area are crucial for ice cloud prediction

Supporting Information:
- Readme
- Figure S1
- Figure S2
- Figure S3
- Figure S4
- Figure S5
- Figure S6
- Text S1
- Movie S1

Correspondence to:
D. A. Knopf,
Daniel.Knopf@Stonybrook.edu

Citation:
Knopf, D. A., P. A. Alpert, B. Wang, R. E. O'Brien, S. T. Kelly, A. Laskin, M. K. Gilles, and R. C. Moffet (2014), Microspectroscopic imaging and characterization of individually identified ice nucleating particles from a case field study, *J. Geophys. Res. Atmos.*, *119*, doi:10.1002/2014JD021866.

Received 7 APR 2014
Accepted 6 AUG 2014
Accepted article online 11 AUG 2014

Microspectroscopic imaging and characterization of individually identified ice nucleating particles from a case field study

D. A. Knopf[1], P. A. Alpert[1], B. Wang[2], R. E. O'Brien[3,4], S. T. Kelly[3], A. Laskin[2], M. K. Gilles[3], and R. C. Moffet[4]

[1]Institute for Terrestrial and Planetary Atmospheres, School of Marine and Atmospheric Sciences, Stony Brook University, Stony Brook, New York, USA, [2]W. R. Wiley Environmental Molecular Sciences Laboratory, Pacific Northwest National Laboratory, Richland, Washington, USA, [3]Chemical Sciences Division, Lawrence Berkeley National Laboratory, Berkeley, California, USA, [4]Department of Chemistry, University of the Pacific, Stockton, California, USA

Abstract The effect of anthropogenic and biogenic organic particles on atmospheric glaciation processes is poorly understood. We use an optical microscopy setup to identify the ice nuclei (IN) active in immersion freezing (IMF) and deposition ice nucleation within a large population of particles collected on a substrate from an ambient environment in central California dominated by urban and marine aerosols. Multimodal microspectroscopy methods are applied to characterize the physicochemical properties and mixing state of the individual IN and particle populations to identify particle-type classes. The temperature onsets of water uptake occurred between 235 and 257 K at subsaturated conditions, and the onsets of IMF proceeded at subsaturated and saturated conditions for 235–247 K, relevant for ice nucleation in mixed-phase clouds. Particles also took up water and nucleated ice between 226 and 235 K and acted as deposition IN with onset temperatures below 226 K, a temperature range relevant to cirrus cloud formation. The identified IN belong to the most common particle-type classes observed in the field samples: organic coated sea salt and Na-rich, secondary, and refractory carbonaceous particles. Based on these observations, we suggest that the IN are not always particles with unique chemical composition and exceptional ice nucleation propensity; rather, they are common particles in the ambient particle population. The results suggest that particle-type abundance and total particle surface area are also crucial factors, in addition to particle-type ice nucleation efficiency, in determining ice formation within the particle population.

1. Introduction

Atmospheric ice nucleation initiated by aerosol particles has important implications for the hydrological cycle and radiative budget, processes that are yet poorly understood [*Baker and Peter*, 2008; *Baker*, 1997]. Mineral dust particles can act as ice nuclei (IN) by initiating immersion freezing (IMF) in supercooled aqueous droplets and deposition ice nucleation (DIN) from the supersaturated vapor phase [*Cziczo et al*., 2013; *DeMott et al*., 2003, 2010; *Hoose and Möhler*, 2012; *Knopf and Alpert*, 2013; *Knopf and Koop*, 2006; *Murray et al*., 2012; *Wang and Knopf*, 2011]. Organic aerosol particles are ubiquitous in the atmosphere [*Heald et al*., 2011; *Zhang et al*., 2007] and thus potentially play a role in atmospheric glaciation processes. This is supported by ice nucleation studies investigating ambient and laboratory organic particles [*Baustian et al*., 2012; *Hiranuma et al*., 2013; *Knopf et al*., 2010; *Murray et al*., 2010; *Wang and Knopf*, 2011; *Wang et al*., 2012a, 2012b]. Previous studies demonstrated that ambient particles, dominated by secondary organic material from anthropogenic environments such as Mexico City (MC) and Los Angeles (LA), can act as IN [*Knopf et al*., 2010; *Wang et al*., 2012b]. Those measurements used computer-controlled scanning electron microscopy with energy-dispersive analysis of X-rays (CCSEM/EDX) and scanning transmission X-ray microscopy with near-edge X-ray absorption fine structure spectroscopy (STXM/NEXAFS) with spatial resolutions of about 5 nm and 30 nm, respectively, in combination with particle population statistical analysis. Furthermore, laboratory studies using secondary organic aerosol (SOA) particles, SOA surrogates, and particles composed of humic acid-like substances corroborate that some of these particle types can act as IN under atmospherically relevant conditions [*Baustian et al*., 2013; *Murray et al*., 2010; *Wang and Knopf*, 2011; *Wang et al*., 2012a; *Wilson et al*., 2012]. This may be due to the organic compounds forming a solid phase below the glass transition points creating a potential IN [*Koop et al*., 2011; *Murray et al*., 2010; *Wang et al*., 2012a].

Table 1. Particle Samples Employed in Ice Nucleation Experiments, Particle Population Characterization, and IN Identification[a]

Particle Sample	$d_{pop}/\mu m$	$N_{part}/\times 10^4$	$A_{tot}/\times 10^{-5}\ cm^{-2}$	$d_{IN}/\mu m$	IN_{ident}	N_{IN}/L^{-1}
SA1	0.55 ± 0.47	$14.7^{+2.9}_{-1.2}$	$27.8^{+56.5}_{-23.9}$	$1.9^{+4.8}_{-1.6}$	25	122
SA2	0.45 ± 0.46	$6.2^{+5.6}_{-5.1}$	$6.6^{+8.1}_{-4.9}$	$1.3^{+4.5}_{-0.9}$	28	82
SA3	0.52 ± 0.43	$3.2^{+4.7}_{-1.0}$	$79.1^{+113.2}_{-45.9}$	$4.5^{+5.5}_{-3.4}$	40	375

[a]SA1 was collected from 10:47 to 12:27 (27/06/10), SA2 from 5:29 to 7:29 (28/06/10), and SA3 from 19:10 to 23:51 (28/06/10). The mean particle population diameter, d_{pop} ($\pm 1\sigma$); range of the particle numbers for ice nucleation, N_{part}; range of the total particle surface area for ice nucleation including uncertainty, A_{tot}; range of IN diameters, d_{IN}; number of identified IN per sample, IN_{ident}; and estimated number of IN per liter of air based on 10^4 particles/cm^3 of air, N_{IN}, are given.

Here we apply methods of optical microscopy (OM), CCSEM/EDX, and STXM/NEXAFS for multimodal chemical imaging of the specific individual particles that acted as IN among an entire population of particles collected from ambient air. This study spans a temperature range of 200–273 K and relative humidity with respect to ice (RH_{ice}) until water saturation is reached, relevant for cirrus and mixed-phase cloud formation in the troposphere and the lower stratosphere. We discriminate specific ice nucleation pathways of individual freezing events, freezing temperatures, and RH_{ice} onsets in relation to the physicochemical properties of detected IN. We then compare the observed IN features with the particle properties of the entire particle population. This allows characterization of the nature of the IN and assessment of whether or not the IN are exceptional compared to the overall particle population. Our approach characterizes individually identified IN from particle samples collected at three different time periods during the Carbonaceous Aerosols and Radiative Effects Study (CARES) field campaign [*Zaveri et al.*, 2012]. The ambient particle population is microspectroscopically characterized using elemental composition cluster analysis, carbon functional group composition, and mixing state analysis [*Moffet et al.*, 2013; *Wang et al.*, 2012b]. The ice nucleation and water uptake onsets are reported along with corresponding ice nucleation pathways. The microspectroscopic characteristics of the identified IN are compared to those of the ambient particle population.

2. Experimental Section

2.1. Particle Collection

Particles in sizes of 0.1–2.5 μm were collected on Si wafer chips (Silson, Inc.), 50 nm carbon films supported on copper grids ("Carbon Type-B" grid substrates, Ted Pella, Inc.), and silicon nitride-coated Si frames ("Si_3N_4-film" substrates, Silson, Inc.) at the T0 ground site (located in urban Sacramento area) using Time-Resolved Aerosol Collectors (TRACs) [*Laskin et al.*, 2003, 2006]. The 50% cutpoint of the TRAC is approximately 0.35 μm. After sample collection, the entire cartridges with particle samples were removed from the TRAC and sealed airtight for storage. Meteorological conditions are described in detail by *Moffet et al.* [2013], and backward trajectories of sampled air mass are given in Figure S1 in the supporting information. Each of the particle samples was collected for 20 min. The collection time periods and particle sample characteristics for the three samples "SA1" (noon), "SA2" (morning), and "SA3" (night) are given in Table 1.

2.2. Ice Nucleation Experiment

The experimental setup has been described in detail previously and is only briefly presented here [*Alpert et al.*, 2011; *Knopf et al.*, 2010, 2011; *Wang and Knopf*, 2011; *Wang et al.*, 2012b]. Selected samples were removed from the TRAC cartridges and installed onto the ice nucleation cell. This installation was done in a particle free laminar flow hood, and particles in the cell remained sealed against ambient air for the duration of the experiment. The onsets of water uptake and ice formation are monitored visually using a controlled vapor cooling–stage microscope system consisting of an ice nucleation cell coupled to an OM. The onsets for water uptake and ice formation reflect the particle temperature (T_p) and RH_{ice} values at which the water uptake (growth of particles) or the first ice crystal was observed [*Wang and Knopf*, 2011]. If multiple ice crystals formed simultaneously, then all the initially formed ice crystals were considered. However, subsequent ice formation events were discarded since a uniform RH field may not persist when ice crystals are present in the ice nucleation cell. This setup allows the control of RH_{ice} and T_p. Humidified N_2 gas (ultrahigh purity) purged through carbon, and cold traps at about 1 standard liter per minute is flown over the particles. Subsequently, the dew point (T_d) is determined using a chilled mirror hygrometer. From T_d and

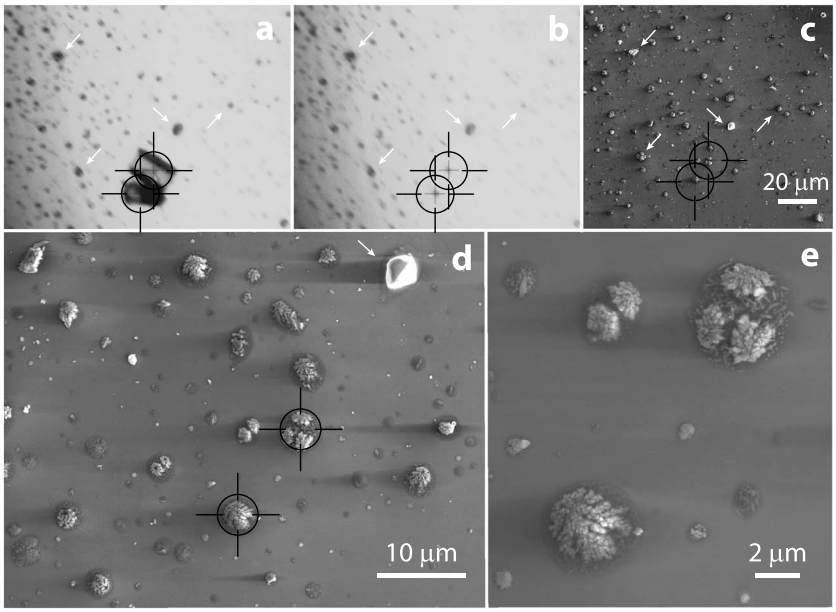

Figure 1. Representative procedure of IN identification for sample SA3. (a) The cross hairs indicate the position of the center of ice crystals initiated by particles of SA3 sample via deposition ice nucleation at $T = 216.3$ K and $RH_{ice} = 135\%$. (b) Sublimed ice crystal after exposure to subsaturated conditions. Figures 1a and 1b are obtained using optical microscopy. (c) The same field of view imaged by scanning electron microscopy (SEM). (d and e) The higher magnification SEM images of the IN. The white arrows point to the same particles in Figures 1a–1d.

T_p, RH_{ice} is determined [*Murphy and Koop*, 2005]. The particles are cooled at a rate of 0.1 K min^{-1} corresponding to an increase in RH_{ice} of about 2.3 to 1.5% min^{-1} for T_p from 200 to 260 K and exposed to ice supersaturation until ice formation or water uptake is observed. Experimental uncertainties are $\Delta T_p < \pm 0.3$ K, $\Delta T_d < \pm 0.15$ K, and $\Delta RH_{ice} < \pm 11\%$ at 200 K and $\Delta RH_{ice} < \pm 3\%$ at 260 K. The onset is defined as the temperature and humidity at which water uptake or ice formation is initially observed. During the entire experiment, images are recorded every 0.02 K (~12 s) along with the corresponding experiment time, T_p, and T_d. For all samples, at least 6 experiments were conducted at each investigated temperature. In total, about 95 ice nucleation experiments were performed. These yielded 93 individually identified IN as indicated in Table 1 that were later probed by SEM/EDX and STXM/NEXAFS to elucidate their morphological and compositional characteristics.

2.3. Identification of Individual IN

Particles acting as IN are identified from two subsequently recorded OM movies of ice nucleation and crystal growth and the ice crystal sublimation. After identification, these specific particles are relocated in SEM/EDX and/or STXM/NEXAFS experiments for microspectroscopic analyses. Figure 1 and Figure S2 in the supporting information illustrate examples of locating the IN. Initially, an ice crystal forms on a single particle as shown in Figure 1a and Figure S2, panels a, in the supporting information. Subsequently, the particle sample is warmed at a rate of 0.5 K min^{-1} and images are taken every 0.1 K until the ice crystal completely sublimates, leaving behind the clearly visible particle that acted as IN (Figure 1b and Figure S2, panels b, in the supporting information). The sublimation and ice formation image sequences are converted to movies and reviewed to spot the IN. An example movie file displaying the ice formation and ice crystal sublimation process is given in the supporting information. Using visual pattern recognition and movie files, the IN are relocated using microspectroscopic imaging techniques as shown in Figure 1c and Figure S2, panels c, in the supporting information. Subsequently, highly magnified and detailed images of the IN, such as those shown in Figures 1d and 1e and Figures S2, panels d and e, in the supporting information, are made in addition to elemental composition analysis using SEM/EDX and chemical imaging by STXM/NEXAFS. When additional accuracy was required to correctly locate the IN, triangulation was used with respect to an arbitrary calibrated point on the sample.

2.4. Particle Analyses

The methods of chemical imaging for field-collected atmospheric particles applied in this study have been described in detail previously [*Gilles et al*., 2010; *Hopkins et al*., 2007a; *Knopf et al*., 2010; *Laskin et al*., 2006; *Moffet et al*., 2010b, 2013; *Takahama et al*., 2007; *Tivanski et al*., 2007; *Wang et al*., 2012b] and are only briefly introduced here. When analyzing a particle with both STXM/NEXAFS and SEM/EDX, STXM/NEXAFS was performed first since SEM/EDX analysis can result in a greater particle damage. For both techniques, a statistically significant number of individual particles were analyzed to yield a representative classification of the various particle-type classes present in the ambient particle population [*Moffet et al*., 2013; *Wang et al*., 2012b]. For example, a sample number of 788 particles yields a representation of the particles collected on the substrate at 99% confidence level with a margin of error of 1% [*Thompson*, 1987]. Note that well over 1000 particles were used in the analyses here. The CCSEM/EDX and STXM/NEXAFS analyses are performed at 1×10^{-5} hPa of air and 500 hPa of helium, respectively, and at room temperature. Therefore, semivolatile organic compounds may have evaporated during analysis. Hence, the organic particle fraction detected can be assumed to have low volatility in nature.

Samples collected on Carbon Type-B substrates were used to conduct CCSEM/EDX analysis over a large particle population. Samples on Carbon Type-B and Si_3N_4-film substrates were used for STXM/NEXAFS analysis. Only samples on Si wafer chips and Si_3N_4-film substrates were utilized for water uptake and ice nucleation studies in the OM experiments [*Knopf et al*., 2010; *Wang et al*., 2012b]. Individual IN identified in these OM experiments were later probed using SEM/EDX and STXM/NEXAFS.

As each sample was collected for 20 min, these substrates represent slightly different sampling periods. Therefore, samples chosen to infer the general particle population characteristics of the air parcel had sampling start times within 1 h of those used for ice nucleation experiments and IN identification. For example, the SA1 samples for ice nucleation experiments were collected at 10:47–11:07 and 12:07–12:27, whereas the SA1 samples for statistical population analysis using STXM/NEXAFS were collected at 10:27–10:47 and 12:27–12:47.

Surface area of individual particles was estimated from SEM images and corroborated using optical and X-ray microscopy. The total particle numbers and the circular equivalent diameters of particles calculated using image analysis software were used to derive the total surface area in a particular field of view approximately 50 μm $\times$ 40 μm. Depending on aerosol loading, the total surface area in about 20–40 representative fields chosen at random locations was determined and used to estimate the total particle surface area residing in the ice nucleation sample area for a single sample.

Water uptake followed by ice formation may alter the particles with respect to chemical composition or morphology. However, this is not expected to deviate significantly from particle characteristics of the overall particle populations. Ice nucleation experiments were always conducted before microspectroscopic analysis. To minimize particle morphological alteration due to the presence of liquid water, experiments were performed first at the lowest achievable temperatures that likely induce DIN. In subsequent experiments, the particle temperature was systematically increased including the occurrence of water uptake and IMF until no ice formation event could be detected. All identified IN inducing IMF and DIN were characterized by SEM/EDX. However, IN characterized by STXM/NEXAFS were only active in DIN. When STXM/NEXAFS data acquisition was not planned on a particle sample, ice nucleation experiments were followed by taking SEM images at low electron beam energies and subsequently acquiring EDX spectra. In most cases, acquiring EDX spectra results in particle damage. However, in spite of undergoing IMF and DIN, their morphology and composition contain identifiable features of the same particle types present in the population, i.e., major particle-type classes that did not nucleate ice. In addition, it is unlikely that a refractory carbonaceous particle will be altered in such a way to reflect a completely different particle-type class such as sea salt as a result of electron beam damage. We conclude that the determined morphology and composition of all the ambient particles, including the identified IN, most likely reflect actual particle properties.

2.4.1. CCSEM/EDX Analysis

CCSEM/EDX provides information on size, morphology, and elemental composition of a large number of individual particles [*Hopkins et al*., 2007a, 2008; *Laskin et al*., 2006, 2012]. The particles are imaged and then the EDX spectra of individual particles are recorded and processed to yield elemental compositions. A SEM

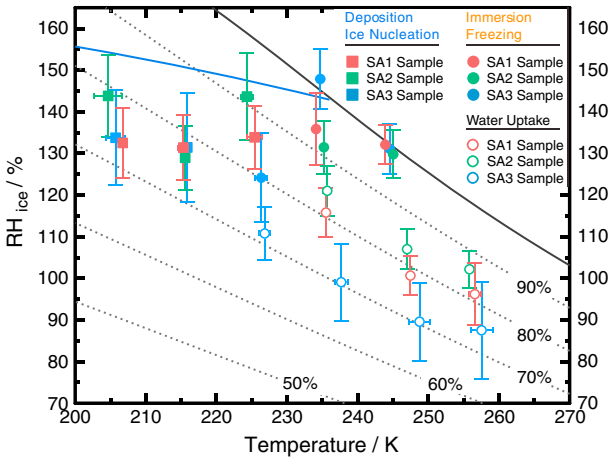

Figure 2. Experimentally determined mean onset conditions (±1σ) of water uptake, immersion freezing, and deposition ice nucleation for particle samples SA1, SA2, and SA3 collected during CARES. The black line represents water saturation. The blue line indicates the homogeneous freezing limit for $J_{hom} = 10^{10}$ cm^{-3} s^{-1} [*Koop et al.*, 2000a]. The dotted lines correspond to constant relative humidity (RH).

(Quanta 3-D model, FEI, Inc.) with a 10 mm^2 Si(Li) X-ray detector (EDAX, Inc.) provided elemental information and atomic ratios of C, N, O, Na, Mg, Al, Si, P, S, Cl, K, Ca, Mn, Fe, and Zn. CCSEM/EDX spectra acquired on thin carbon films were quantified using the Genesis^{TM} software for X-ray analysis (EDAX, Inc). Particles with an equivalent circle diameter larger than 0.2 μm were characterized. Additional information on the applied methods are published elsewhere [*Laskin et al.*, 2003, 2006; *Moffet et al.*, 2008, 2010a].

For each sample, atomic fractions of thousands of individual particles were clustered following a *k*-means analysis. The *k*-means cluster analysis generates *k* different atomic ratio spectra aimed to converge on average spectra for *k* groups of particles. In other words, *k*-means effectively assigns the atomic fraction spectrum of a single particle to 1 of *k* different average spectra [*Cheng*, 1995; *Fukunaga and Hostetler*, 1975; *Selim and Ismail*, 1984]. The particle data analyzed here were combined with those presented by *Moffet et al.* [2013], and seven clusters ($k = 7$) were used to characterize all particles into clusters belonging to fine mode (<1 μm in diameter) and coarse mode (>1 μm) particles. Clusters were named based upon visually distinct and recognizable particle features, and their SEM/EDX determined atomic fraction spectra. Recognizable features included fractal soot on the order of 100 nm in diameter, sea salt particles containing Na and Mg, as well as other more general descriptions such as carbonaceous.

2.4.2. SEM/EDX of Individual IN

Individually identified IN on Si wafer chips were analyzed manually by SEM/EDX to obtain SEM images and EDX spectra. The background substrate correction was employed for each particle. This was done by subtracting a "substrate-only" spectrum acquired on a particle-free region adjacent to the individually analyzed particle under identical experimental conditions. In this way, each particle had its own background substrate correction. The atomic fractions of the major elements of the IN were then computed. By combining the visual inspection with the atomic fractions, individual IN were assigned to specific clusters.

2.4.3. STXM/NEXAFS Analysis

STXM measures the transmission of soft X-ray beams generated from the synchrotron light source across a raster-scanned sample at a given photon energy to obtain an image [*Kilcoyne et al.*, 2003]. Spatially resolved X-ray spectra yield chemical composition and mixing states of individual particles [*Hopkins et al.*, 2007a, 2008; *Michelsen et al.*, 2007; *Takahama et al.*, 2007; *Tivanski et al.*, 2007]. The spatial resolution was 25 nm. Exploiting the carbon K-edge spectra allows the identification of organic carbon (OC), elemental carbon (EC, i.e., soot), potassium (K), and other overall contribution of inorganic components (INO) within individual particles. The presence of calcium (Ca) was determined by exploiting the Ca L-edge [*Benzerara et al.*, 2004; *Rieger et al.*, 1986]. This will allow to classify particle types and their respective mixing state using STXM/NEXAFS. An overview of the application of this technique to atmospheric particles and technical details on STXM are published elsewhere [*Ghorai et al.*, 2011; *Ghorai and Tivanski*, 2010; *Gilles et al.*, 2010; *Moffet et al.*, 2010a, 2010b].

3. Results and Discussion

3.1. Onsets of Water Uptake, Immersion Freezing, and Deposition Ice Nucleation

Figure 2 shows the water uptake, IMF, and DIN onsets obtained for samples SA1 (noon), SA2 (morning), and SA3 (night). Initial water uptake commences at subsaturated conditions at temperatures as low as 226 K. Particles from the SA3 sample exhibit the lowest onsets of water uptake, around 70–75% RH. For $T > 236$ K, SA1 and SA2 particle samples exhibit water uptake around 80 and 85% RH, respectively. Particles of the SA3 samples induce IMF at lowest temperatures, i.e., at 226 K at 80% RH. At higher temperatures, IMF occurs at

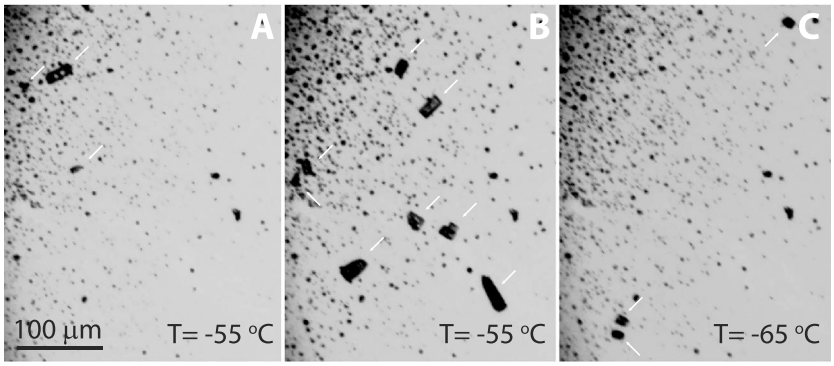

Figure 3. Optical microscopy images of three ice nucleation experiments conducted with the same SA3 particle sample at (a and b) -55°C and (c) -65°C. Figures 3a and 3c show the experiments conducted repeatedly after experiment (Figure 3a). Between subsequent experiments, the sample was heated to >0°C and RH~0% for 5 min to allow complete sublimation of the ice crystals.

saturated conditions. SA2 and SA1 particles initiate IMF at about 132% RH_{ice}, which coincides with water saturation at higher temperatures. DIN was observed for $T < 226$ K and RH_{ice} of about 133%, 140%, and 133% for SA3, SA2, and SA1 particle samples, respectively. These onsets are about 20% lower in RH_{ice} compared to the homogeneous ice nucleation limit [*Koop et al.*, 2000a].

Similar to our previous ice nucleation studies employing ambient organic and laboratory-generated organic particles, we observed that repetition of an ice nucleation experiment using the same particle sample and identical thermodynamic conditions (i.e., temperature and RH) resulted in different particles initiating ice formation [*Knopf et al.*, 2010; *Wang et al.*, 2012a, 2012b]. These observations are illustrated in Figure 3, which indicates that within the same sample, ice crystals are typically formed on different particles in consecutively repeated experiments. After observation of an ice formation event, the particles are held at 275 K for at least 5 min and RH < 1% for complete ice crystal sublimation. Subsequently, the sample is cooled again to the desired experimental particle temperature, but kept above T_d to ensure subsaturated conditions with respect to ice. By cooling further with the same rate (i.e., 0.1 K min^{-1}) as in the initial experiment, the ice nucleation experiment is repeated. Different particles acting as IN in repeated experiments were a prevalent feature for both DIN and IMF. As indicated in Figure 3, if the experiment is repeated at a different temperature, also different particles act as IN. These observations are in contrast when employing the surrogates of mineral dust such as Arizona test dust (ATD) and kaolinite particles, for which in subsequent repetitions of the ice nucleation experiments, the same most efficient IN nucleate ice multiple times [*Knopf and Koop*, 2006; *Wang et al.*, 2012a]. The repetition of the ice nucleation experiments involving ATD can lead to the enhancement of the particles' ice nucleation ability due to preactivation [*Knopf and Koop*, 2006].

3.2. Particle Population Characteristics Obtained by CCSEM/EDX

We characterize the particle population characteristics of samples SA1, SA2, and SA3 by applying the cluster analysis scheme reported in our previous work [*Moffet et al.*, 2013] and shown in Figure 4. The *k*-means cluster analysis applied atomic ratios of C, N, O, Na, Mg, Al, Si, P, S, Cl, K, Ca, Mn, Fe, and Zn elements. Figure 4a shows the derived *k*-means clusters for the investigated sampling periods. Generally, particle clusters similar to those measured by *Moffet et al.* [2013] at the T0 site were observed.

1. *Cluster 1: aged sea salt (mostly coarse mode particles)*. Characterized by high atomic percentage of Na, Mg, K, and Ca. In addition, significant S is present, and Cl is depleted. Cl depletion could be due to displacement by reaction with weak organic acids [*Laskin et al.*, 2012], nighttime hydrolysis of N_2O_5 [*Knopf et al.*, 2007; *Thornton et al.*, 2010] and subsequent $ClNO_2$ formation [*Fenter et al.*, 1996; *Thornton et al.*, 2010], or HNO_3 uptake and subsequent HCl release [*Beichert and Finlayson-Pitts*, 1996; *Fenter et al.*, 1994]. Although predominantly coarse mode, this cluster manifests a significant portion of particles below 1 μm in diameter.
2. *Cluster 2: carbonaceous Na-rich (mostly fine mode particles)*. Characterized by a dominant contribution of carbon. The second most abundant elements are O, Na, and S. Although defined as fine mode, this particle type also contributes significantly to the coarse mode particle population.
3. *Cluster 3: secondary carbonaceous (fine mode particles)*. Characterized by a dominant contribution from carbon. The second most abundant element is O, followed by N and S. Compared to the other fine

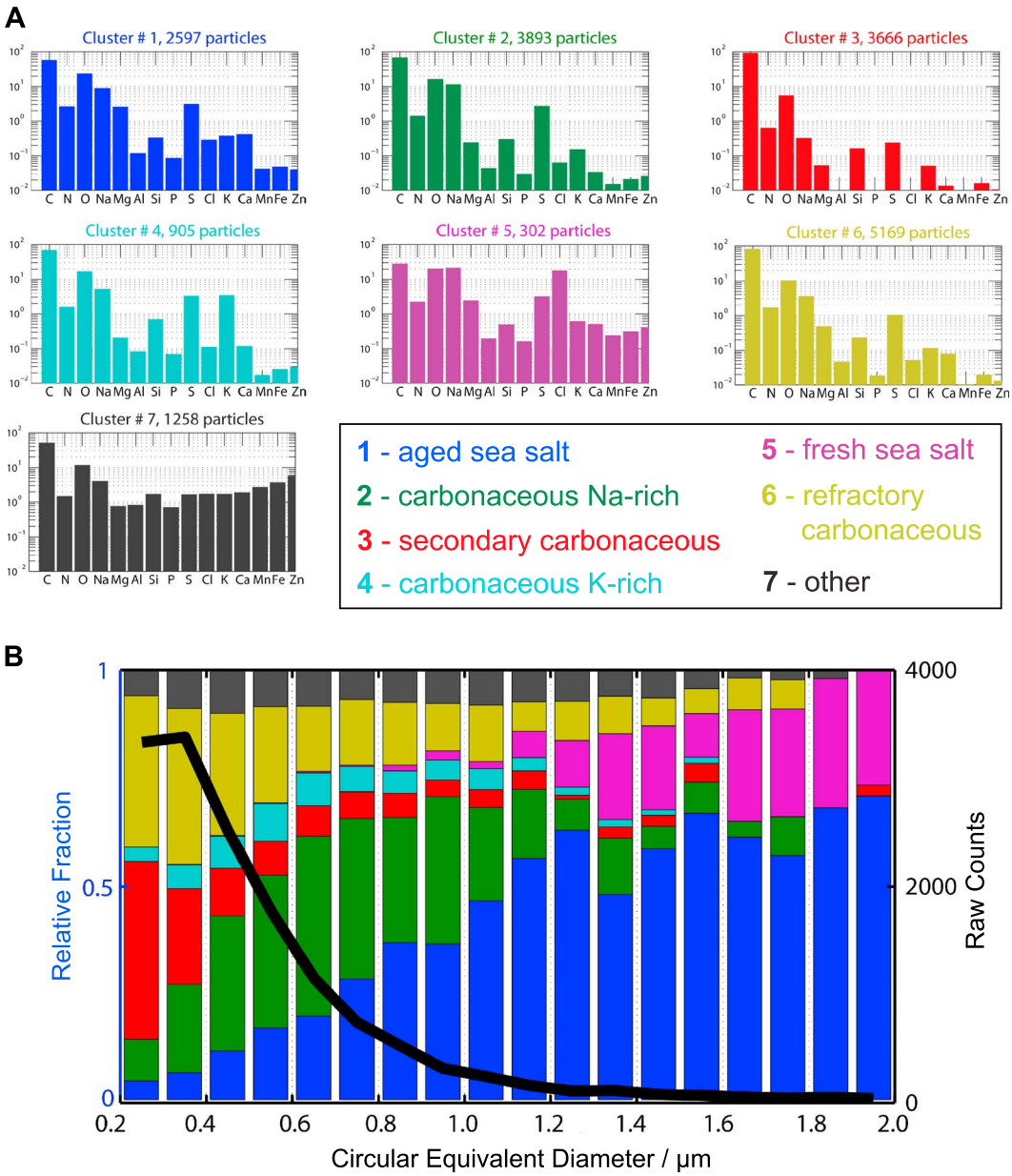

Figure 4. Summary of *k*-means cluster analysis using CCSEM/EDX data for particles collected at the T0 site. (a) Mean EDX spectra for each of the derived clusters. (b) Fractions (left axis) of the different clusters as a function of particle size. The solid line represents the total counts of all particles (right axis).

mode clusters, this cluster has much less influence from elements other than O. This cluster is labeled "secondary" due to the lack of trace elements that typically indicate a primary "particle core" containing nonvolatile elements.

4. *Cluster 4: carbonaceous K-rich (fine mode particles)*. Characterized by a dominant contribution of carbon with the second most abundant elements of K, O, Na, and S. These particles potentially have a Na-dominated core.
5. *Cluster 5: fresh sea salt (mostly coarse mode particles)*. Characterized by high atomic fractions of Na, Mg, and Cl. Although carbonaceous material is present, it is less than for other clusters.
6. *Cluster 6: refractory carbonaceous (fine mode particles)*. This cluster has an enhanced contribution from metallic elements (Na, Mg, Ca, Fe, and K) and Cl in addition to large contributions from C, N, and O.

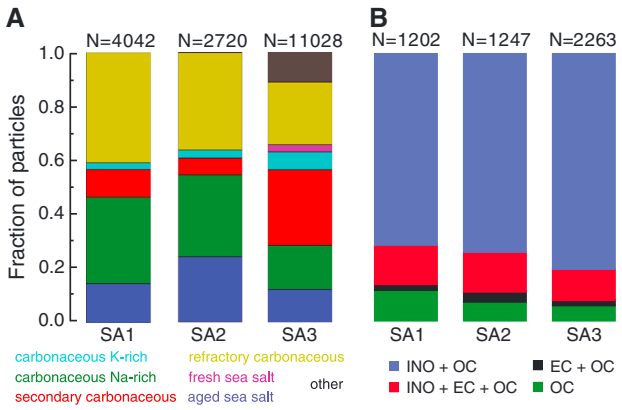

Figure 5. Fractions of particle-type classes with respect to (a) composition and (b) mixing states present in ambient aerosol population as determined by CCSEM/EDX (Figure 5a) and STXM/NEXAFS (Figure 5b) for the SA1, SA2, and SA3 samples. The identified particle-type classes are given in respective color. Particles consist of organic carbon (OC), inorganics (INO), and elemental carbon (EC) and are classified into the following types INO + OC, INO + EC + OC, EC + OC, and OC. The total number of analyzed particles for each sample, *N*, is shown at the top.

These particles could be mixtures of sea salt or cooking emissions that have been coated with secondary organic species. This cluster also contributes to coarse mode particles.

7. *Cluster 7: other (fine mode particles).* About 7.1% of all analyzed particles fall into this category. Large amounts of refractory material are present, and their source is not clear. In some cases, a significant noise is misinterpreted as peak by the quantification algorithm, possibly from the edges of the underlying copper grids or the sample holder and are thus artifacts in the analysis.

Figure 4a shows that all identified particle clusters contain significant contributions of carbon and oxygen. This is consistent with SEM particle images indicating the presence of organic material as a greyish shading and with STXM/NEXAFS analysis as discussed below. The coarse mode particles contain larger amounts of Na, Cl, Mg, K, or Ca, indicative of a marine source, compared to the fine mode particles. The smaller particles are dominated by carbon and oxygen with varying amounts of refractory material.

Figure 4b shows the relative contribution of each derived cluster in 100 nm size bins ranging from 200 nm to 2 μm. The maximum numbers of particles reside in a size range of about 300 nm. Below 400 nm, the population is dominated by secondary and refractory carbonaceous particles contributing about 40 and 30%, respectively, of all particles. Particles with 400–1000 nm diameters are primarily carbonaceous Na-rich and aged sea salt and contribute to about 35 and 40%, respectively, of the total particle numbers. The carbonaceous Na-rich particles may stem from the same source as the coarse mode aged sea salt particles; both show a strong depletion of Cl. However, the larger aged sea salt particles are enriched in Mg compared to the fine mode Na-rich particles. The refractory carbonaceous particle cluster may also stem from a marine source and hence contribute to particle diameters above 1 μm [*Moffet et al.*, 2013]. The aged and fresh sea salt particles dominate the coarse mode population making up about 60 and 35%, respectively, of the particles 1–2 μm in diameter.

Figure 5a shows the averaged fractions of the particle-type classes for each of the three sampling periods for all particle sizes. SA1 and SA2 sampling periods are dominated by Na-rich carbonaceous, aged sea salt particles, and refractory carbonaceous particles, all of which may have been influenced by sea spray. Additionally, secondary carbonaceous particles are about 10% of the total particle number. The SA3 samples contain a significant number of particles likely affected by a marine source. Fresh sea salt, aged sea salt, and Na-rich particles represent more than 30% of all particles. Furthermore, the refractory carbonaceous particles may also be related to sea spray emissions. SA3 samples contain a higher amount of secondary carbonaceous particles compared to the SA1 and SA2 samples. The backward trajectories (Figure S1 in the supporting information) suggest that the air mass containing SA3 samples resided longer over continental areas, thus possibly allowing for an increased amount of photochemically produced secondary organic material to condense onto particles.

3.3. Particle Population Characteristics Obtained by STXM/NEXAFS

We apply STXM/NEXAFS to characterize the carbon composition and mixing state of particles in the ambient population. Figure 6 shows the representative STXM/NEXAFS component images and corresponding averaged X-ray spectra indicating the spatial distributions of major components identified at the carbon K-edge for the three sampling periods. X-ray images at 278, 285.1, and 288.7 eV provide optimum contrast for non-carbonaceous inorganic species (pre-edge below carbon absorption), soot peak (C = C), and the COOH peak (organic carbon), respectively [*Hopkins et al.*, 2007a, 2007b; *Moffet et al.*, 2010a, 2013; *Takahama et al.*,

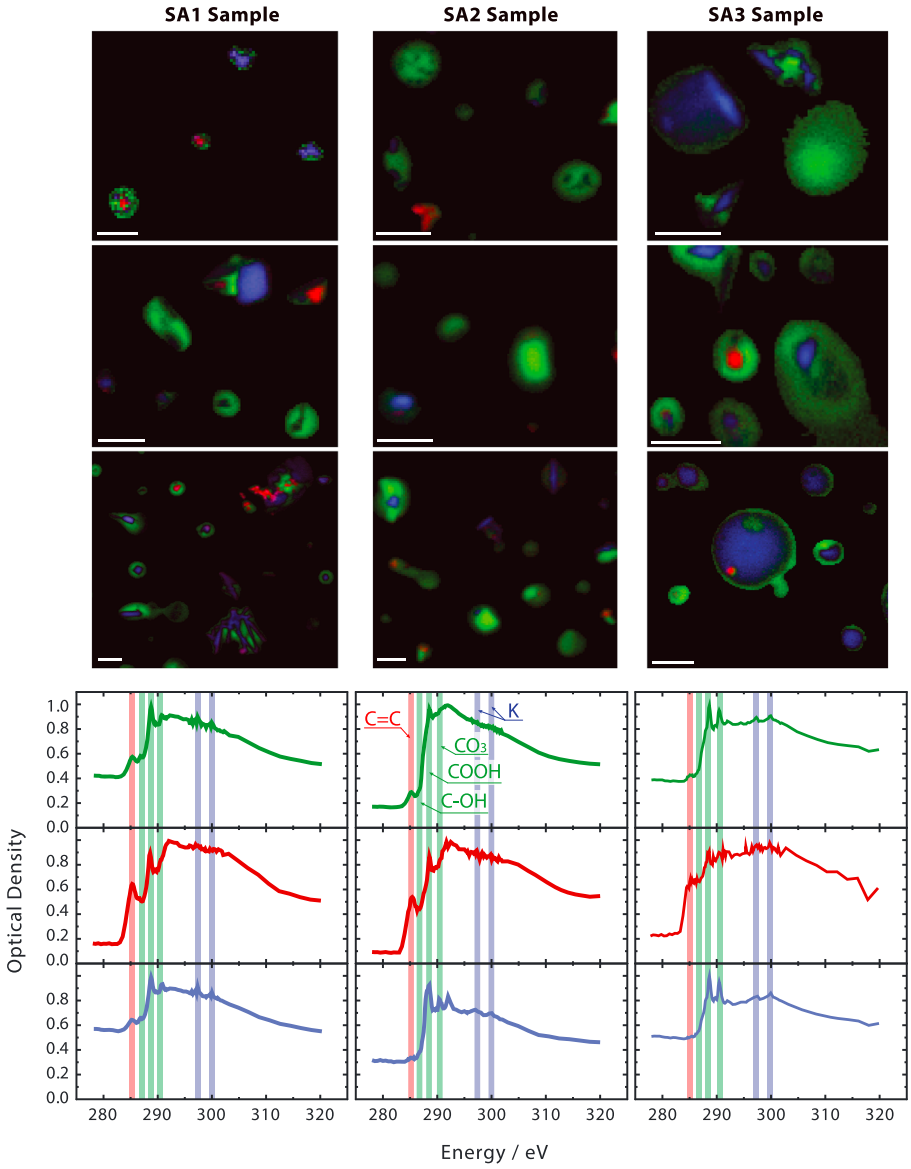

Figure 6. (top) Component images and (bottom) corresponding normalized X-ray spectra for the SA1, SA2, and SA3 samples. In each of the component images, the green, red, and blue colors map the dominating presence of the carboxyl functional group (organic material), carbon double bonding (soot-like), and inorganic material, respectively. The X-ray spectra below each component map represent the mean spectra for that sample obtained from the regions dominated by organic (green), soot-like (red), and inorganic materials (blue), respectively. The scale bars are 1 μm. The spectra are normalized to their maximum optical density values.

2007]. The green, red, and blue color maps and the corresponding averaged X-ray spectra represent the dominating presence of the organic material (featured by carboxyl functional groups), soot-like refractive carbon (featured by C = C double bonds) and overall inorganic material (inferred from differences in absorption at post-edge and pre-edge enegy levels), respectively, for all particles imaged. These component images show that the particles are associated with and coated by organic carbon independent of the sampling period. This corroborates our findings based on CCSEM/EDX. The corresponding averaged X-ray spectra indicate the presence of carboxylic functionalities in the particle regions dominated by soot-like and inorganic materials. For example, within the inorganic-dominated particle fraction (blue colored), the corresponding X-ray spectra always contain a significant peak indicative of the −COOH groups. This further corroborates the previous point that these particles are engulfed by organic material. The averaged X-ray spectra also show the minor presence of OH functionalities (at 286.5 and 287.0 eV), carbonates (at 290.4 eV),

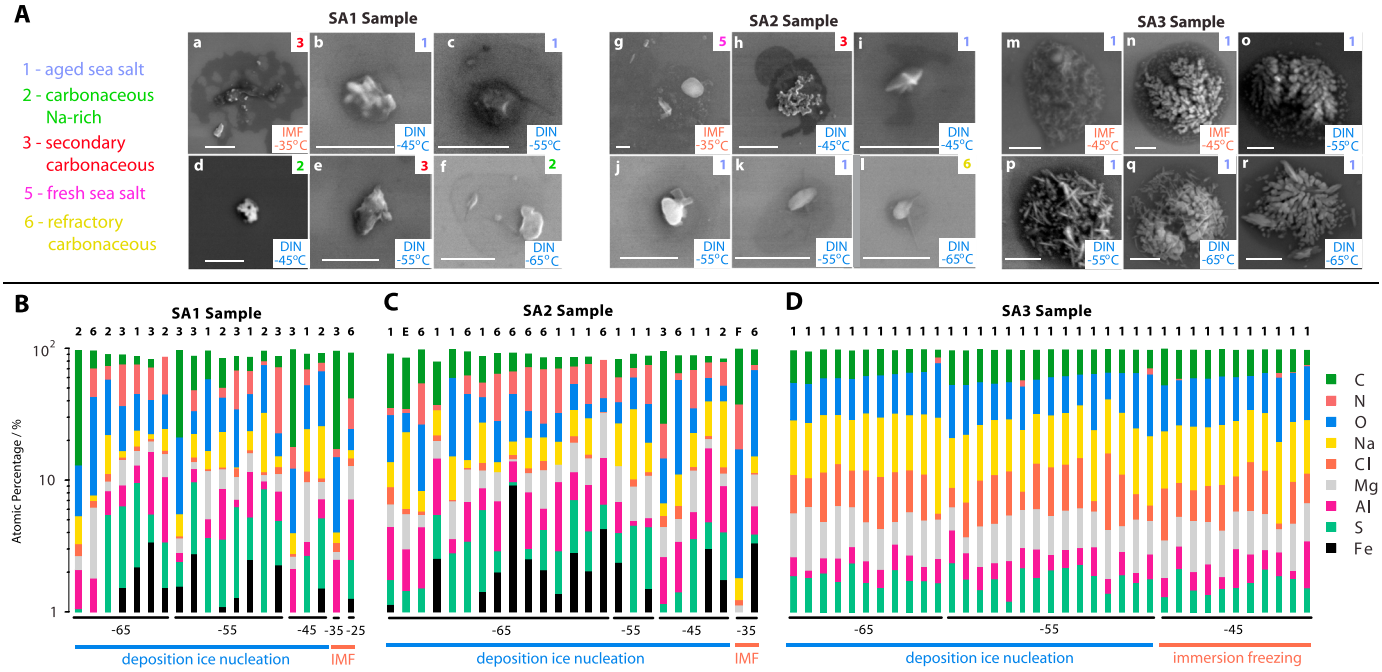

Figure 7. Images and composition of experimentally identified IN. (a) SEM images of representative IN identified from SA1 (images a–f), SA2 (images g–l), and SA3 (images m–r) samples. The observed ice nucleation pathway, immersion freezing (IMF), or deposition ice nucleation (DIN) is given in the bottom right corner of each image with the onset freezing temperature. For each particle, a cluster assignment is given in the top right corner of the image. All the scale bars indicate 1 μm. (b–d) Cumulative atomic percent of elements for 82 identified individual IN are shown as bars for the SA1 (Figure 7b), SA2 (Figure 7c), and SA3 (Figure 7d) samples as a function of their ice nucleation onset temperatures and ice nucleation pathways. At the top of each bar, the cluster assignment is given. Letters E and F within Figure 7c indicate the presence of biological particles associated with brochosomes and spores or pollen grains, respectively.

and potassium (at 299.7 and 297.1 eV) [*Hopkins et al.*, 2007b; *Moffet et al.*, 2013; *Takahama et al.*, 2007]. Particles from SA3 sample exhibit the strongest carbonate signal, whereas particles from SA2 and SA1 samples show higher contributions of soot-like compounds.

Figure 5b shows the composition and internal mixing state of all investigated ambient particles for each sampling period following the methodology of previous studies [*Knopf et al.*, 2010; *Moffet et al.*, 2013; *Wang et al.*, 2012b]. The following particle types are discriminated [*Moffet et al.*, 2010a]: (i) Organic carbon (OC): these particles have a dominant organic composition by mass homogeneously distributed throughout the entire particle. (ii) EC + OC: regions of these particles have high C = C sp^2 hybridized bonds along with organic functional groups. The percentage of sp^2 bonds required for a particle to be designated with an EC component is greater than 35% [*Hopkins et al.*, 2007a]. (iii) INO + OC: these particles have an inorganic inclusion in addition to organic material. (iv) INO + EC + OC: particles having inorganic dominant regions, soot regions, and organic regions according to above given specifications.

Figure 5b illustrates that the largest fraction of particles belong to the class INO + OC. No bare soot, bare sea salt, or bare refractory particles are present in the population; all particles are internally mixed with organic material and an organic coating. These observations are independent of the different sampling time periods and corroborate the results from the CCSEM/EDX analysis. However, CCSEM/EDX analysis suggests a larger fraction of OC particles (secondary carbonaceous) present in the SA3 sample compared to the results of STXM/NEXAFS. It should be noted that the secondary carbonaceous cluster also includes elements other than O and C, and thus, direct comparisons may not be possible. Furthermore, the investigated particle populations exhibit the same compositional, morphological, and mixing state features as the airborne particles sampled at the same location a few days prior [*Laskin et al.*, 2012].

3.4. Individual IN Characteristics Probed by SEM/EDX

Figure 7a displays the representative SEM images of 18 identified IN and corresponding freezing temperatures, ice nucleation pathways, size, and assigned *k*-means cluster numbers of the total ambient particles for each sampling period. The IN of the SA1 sample are carbonaceous and aged sea salt particles

(images a–f of Figure 7a). Although not apparent by visual inspection, the IN of image a are entirely carbonaceous. The IN of the SA2 sample (images g–l of Figure 7a) are dominated by aged sea salt particles and refractory carbonaceous particles. The IN displayed in images k and l exhibit very similar morphologies possessing a core with a spine surrounded by organic material. However, the elemental composition analysis resolves that these IN are aged sea salt and refractory carbonaceous particles, respectively. The IN of the SA3 sample (images m–r of Figure 7a) are dominated by supermicron aged sea salt particles that are depleted in Cl and show similarities in morphology to particles of marine origin [*Laskin et al*., 2012]. The IN from the SA3 sample are larger than those from the SA1 and SA2 samples. All identified IN possess a core surrounded by organic material which also represents a key feature of the ambient particle population as determined by CCSEM/EDX and STXM/NEXAFS.

The SEM/EDX-derived IN compositions, shown in Figures 7b–7d, are expressed as cumulative atomic fractions. Figures 7b–7d also show corresponding ice nucleation pathways, freezing temperatures, and associated *k*-means cluster numbers. It is important to note that the substrates used here have no C background associated with them. Although the absolute quantification of C is very challenging using EDX, the positive presence of carbon can be detected and relative intercomparisons between different particles can be made.

The general conclusions for all investigated IN that can be drawn from Figure 7 are the following: all particles are associated with C, making C the most likely abundant element, followed by N and O (this is similar to measured population characteristics); there are no clear trends in IN composition with regards to freezing temperatures and ice nucleation pathways; and all identified IN, within their size range, belong to a major particle-type class typical of this sampling period. This analysis suggests that in terms of chemical composition, the IN are not significantly different from the majority of the particles in the population at this sample site and for the IN processing conditions represented. Lastly, for all sampling periods and in the majority of the cases (with the exception of fresh sea salt particles), the IN are depleted in Cl relative to Na. Only two plausibly biological particles were identified: grasshopper brochosomes [*Wittmaack*, 2005] (Figure S2b in the supporting information) and a spore or pollen grain (Figure S2c in the supporting information). We cannot infer whether the brochosomes themselves or the particle (Na-rich carbonaceous) to which the brochosomes are attached initiated ice nucleation. The supermicrometer-sized spore or pollen induced IMF.

Closer inspection of Figures 5 and 7 indicates that the IN of the samples consist of secondary carbonaceous, Na-rich carbonaceous, aged sea salt, and refractory carbonaceous particles. These particle-type classes represent major fractions, of about 10 to 40%, of all particles of the investigated populations. From this we can conclude that the IN in our samples belong to common particle-type classes rather than being exceptional in their composition or morphology.

In general, the IN of all the sampling periods presented in Figure 7 exhibit a core surrounded by organic material. This is shown in more detail in Figure S3 in the supporting information displaying a SEM/EDX-derived elemental map of an aged sea salt particle (sample SA3) acting as IN. These elemental maps demonstrate the depletion of Cl compared to Na and the presence of C at the interface of the solid inorganic core. For reference, Figure S4 in the supporting information shows a SEM image and elemental maps of particles from the SA3 sample which did not nucleate ice. Those particles exhibit similar morphology and composition as the identified IN of this sampling period, including the Cl depletion and the presence of an organic coating. Figure S4 in the supporting information also demonstrates that the IN are not necessarily the largest particles in the population.

3.5. Individual IN Characteristics Obtained by STXM/NEXAFS

Figure 8 demonstrates the experimental capability to use Si_3N_4 substrates for ice nucleation experiments and then to identify and chemically image the IN. The same IN of sample SA3 was further characterized using SEM/EDX by means of elemental mapping (Figure S3 in the supporting information). Figures 8d–8f present the STXM/NEXAFS component images of the IN and non-ice nucleating particles, respectively, and the corresponding averaged NEXAFS spectra are shown in Figure 8g. The green, orange, and blue color maps indicate the dominating presence of the carboxyl functional group, calcium, and the overall inorganic material, respectively. The component image demonstrates that the ice nucleating particle contains an inorganic core surrounded by organic material. The non-ice nucleating particles are of similar size, located close to the IN, and exhibit nearly identical compositional and mixing state features as the IN. Furthermore,

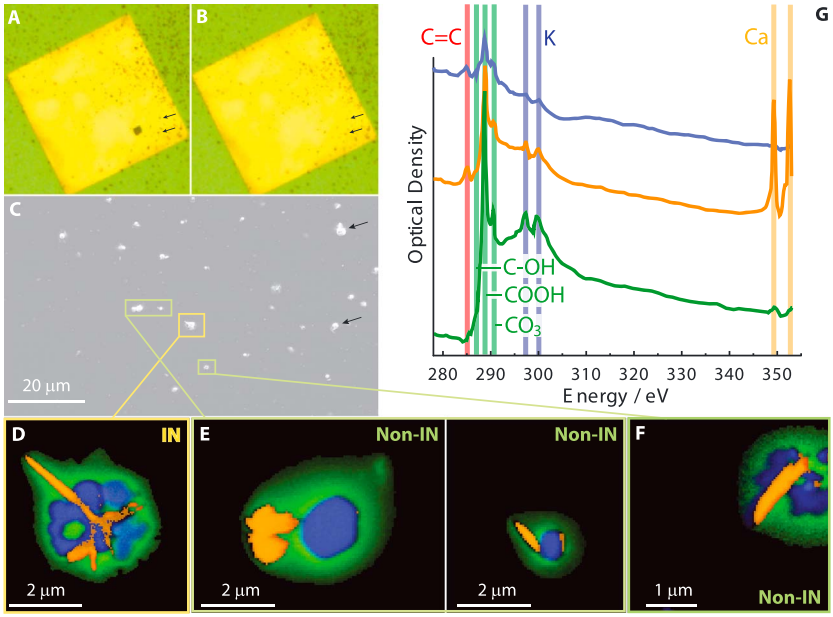

Figure 8. IN identification and STXM/NEXAFS chemical imaging of particles in SA3 sample. (a and b) The ice formation and ice sublimation events observed in the OM experiment, respectively. (c) SEM image of the same sample area at higher magnification. (d) The identified IN and panels (e and f) show non-ice nucleating particles component images emphasizing the contrast between non-carbonaceous inorganic species (blue), organic carbon (green), and calcium (orange). (g) The corresponding NEXAFS spectra of the particles with the major functionalities highlighted. The black arrows point to the same particles. The identical IN, analyzed by SEM/EDX, is illustrated in Figure S3 in the supporting information.

the IN active and the inert particles appear to be very similar in morphology to particles that are abundant in the sample (see, e.g., Figure 1 and Figure S4 in the supporting information and *Laskin et al.* [2012]). Closer inspection of the NEXAFS spectra (Figure 8g) indicates that the particle material has minor contributions of OH functionalities and CO_3 (290.4 eV). The presence of peaks at 346.2 and 349.7 eV from Ca is visible in the corresponding orange spectrum (Figure 8g) taken at the Ca L-edge in agreement with the SEM/EDX elemental maps showing the presence of Ca (Figure S3 in the supporting information). That spectrum also shows the presence of potassium at 299.7 and 297.1 eV and of carboxylic functionalities implying that the calcium is coated with organic material not visible in the component image (Figure 8e). As inferred from the component images and spectra in Figure 8, the mixing state of this IN is INO + OC, exhibited by most particle-type classes. The elemental maps shown in Figure S3 in the supporting information imply that the IN is an aged sea salt particle type, which falls into the INO + OC mixing state category and represents the most common particle type in this sample. In addition, the particle is coated with organic carbon, further corroborating the potential role of organic material in initiating ice nucleation for the cases examined in this study.

The great majority of the IN include the inorganic and organic materials reflecting particles with the mixing state of INO + OC or INO + EC + OC and only 9 of the 83 IN are secondary carbonaceous corresponding to OC or EC + OC particles. The distribution of IN types with regards to composition and mixing state reflects the distribution of particle types within the population. These results further support the notion that the IN belong to major particle-type classes.

3.6. Relating Ice Nucleation With Particle Population and Individual IN Characteristics

The determined physicochemical characteristics of the individual IN and particle populations are applied to examine the observed water uptake and ice nucleation onsets and pathways shown in Figure 2. Particles from the SA3 sample are associated with highest NaCl content compared to the particles from SA1 and SA2 samples (see, e.g., Figure 7 and Figures S3 and S4 in the supporting information). Those particles exhibit the lowest onsets of water uptake, around 70–75% RH, which may be expected from previous deliquescence studies of pure NaCl and sea salt particles [*Koop et al.*, 2000b; *Liu et al.*, 2008; *Wise et al.*, 2009]. Particles of the SA3 sample induce IMF at lowest temperatures, i.e., at 226 K at 80% RH. At higher temperatures, IMF occurs at saturated conditions. Similarly, particles of the SA2 and SA1 samples initiate IMF at lower RH at lower temperatures and at

higher RH at higher temperatures. The reason for this trend may be twofold. First, the water activity IMF model based on classical nucleation theory demonstrates, keeping all other parameters the same, that at higher temperatures, higher RH is necessary to induce IMF compared to at lower temperatures [*Knopf and Alpert*, 2013]. Second, a difference in the viscosity of the organic material acting as IN may be another reason for different IMF onsets, where at low temperatures, a higher particle viscosity and at higher temperatures, a lower particle viscosity dominate [*Wang et al*., 2012a]. Particle viscosity impacts the plasticizing effect of water, i.e., the ability of water penetrating the particle and decreasing particle viscosity, and thus water uptake [*Koop et al*., 2011; *Wang et al*., 2012a]. Both effects could explain the observed IMF onsets.

Table 1 gives the mean IN diameter derived from SEM and indicates that particles >0.3 μm in diameter acted as IN. It should be noted that the particles deposited on substrates may flatten and appear larger in diameter than those that existed in the atmosphere. As demonstrated in the SEM population images (Figure 1 and Figures S2 and S4 in the supporting information), the IN are not necessarily the largest particles present on the sample substrates. These findings are consistent with observations indicating that IN active in the cirrus and mixed-phase cloud regimes are >0.1 μm [*Cziczo et al*., 2013; *DeMott et al*., 2003] and >0.5 μm [*DeMott et al*., 2010], respectively. However, the total particle surface area may also be an important factor in determining ice nucleation onset. Table 1 gives the ranges of the total number of particles (N_{part}) and the total surface areas available in the ice nucleation experiments conducted over 1 mm^2 of the investigated substrate area. The SA1 sample had the largest number of particles on ice nucleation samples, compared with the SA2 and SA3 periods. However, SA3 samples had the largest surface area available for ice nucleation. This could be due to the larger number of coarse mode particles present as demonstrated in the SEM images given in Figure 1 and Figures S2 and S4 in the supporting information. Previous studies indicated that an increase in the total particle surface area decreases the RH_{ice} required to observe ice nucleation [*Kanji et al*., 2008; *Knopf and Alpert*, 2013]. However, the data presented here do not demonstrate such a trend, presumably due to the small range of the total particle surface areas investigated and the experimental uncertainty in RH_{ice}.

We provide an estimate of the number of activated IN per liter of air, N_{IN}, as given in Table 1. This estimate should be regarded with caution because not all particles in the air were sampled due to the cutpoint of the TRAC. We assume typical urban particle concentrations of ~10^4 cm^{-3} [*Seinfeld and Pandis*, 1998]. N_{IN} is derived from the observed activated fraction of IN, i.e., N_{part}^{-1}, and the total particle concentration per liter of air. This yields N_{IN} of 122, 82, and 375 L^{-1}, for samples SA1, SA2, and SA3, respectively. For more or less particles present in the atmosphere, N_{IN} will scale accordingly. These values are within the range of N_{IN} determined in previous field measurements [*DeMott et al*., 2010]. The N_{IN} derived here may be higher compared to N_{IN} values for the free troposphere since the total particle concentration in an urban environment is usually higher.

The occurrence of different particles acting as IN in repeated experiments may be due to the homogeneitity of organic material present on all particles which provides a somewhat uniform surface for ice nucleation in which the stochastic nature of ice nucleation dominates. In this way, ice nucleation occurs randomly for all particles. Another reason may be due to the morphological changes of the particle surfaces as the organic particle phase experiences changes in viscosities and possibly glass transition, when being cycled through a wide range of temperatures and RH [*Adler et al*., 2013; *Wang et al*., 2012a]. In each of these cycles, the organic phase may solidify in a different manner, potentially changing particle surface area, resulting in different ice nucleation activities for each experimental run. *Wang et al.* [2012a] found a similar behavior for laboratory-generated SOA and other organic particles however not for mineral dust particle surrogates such as kaolinite. When repeating an ice nucleation experiment involving ATD particles, *Knopf and Koop* [2006] observed that the same most efficient ice nucleating particle initiated ice formation and furthermore became preactivated. These previous studies combined with the current study suggest that the nature of their organic coating may control ice nucleation occurring on different particles from experiment to experiment.

Water uptake, IMF, and DIN are compared with previously investigated ambient particles collected in urban areas of Mexico City (MC) [*Knopf et al*., 2010] and Los Angeles (LA) [*Wang et al*., 2012b] and laboratory-generated SOA particles [*Wang et al*., 2012a] in Text S1 and Figures S5 and S6 in the supporting information. Briefly, the water uptake, IMF, and DIN onsets of the CARES samples are similar to the ones observed for MC, LA, and SOA particles. One exception is the lowest water uptake onset observed for the SA3 sample of this study, which is probably due to the high NaCl content as discussed above. The total particle surface areas

available for ice nucleation on samples from MC and LA were 0.5×10^{-3} cm^{-2} and $(0.9–2.6) \times 10^{-3}$ cm^{-2}, respectively. The samples of this study exhibit particle surface areas of $(0.06–0.79) \times 10^{-3}$ cm^{-2}, being different by about 1 order of magnitude. Because the ice nucleation onset RH_{ice} between these studies are similar, the particles investigated here may be slightly more efficient IN. To better evaluate this, ice nucleation experiments employing variable total particle surface areas should be employed in future studies [*Kanji et al*., 2008; *Knopf and Alpert*, 2013]. SOA particles generated from naphthalene oxidation show similar water uptake and IMF onsets and had surface areas of $(0.11–0.54) \times 10^{-3}$ cm^{-2} similar to those employed in the experiments of this study. However, CARES samples exhibit slightly lower onsets with respect to RH_{ice} for DIN compared to the laboratory-generated SOA particles, again implying a greater ice nucleation efficiency.

The results in Figure 2 suggest that the ambient organic-dominated particles collected during CARES can participate in cloud formation processes at cold temperatures. The ice nucleation onsets for these organic particles, in particular for DIN, are likely higher with respect to RH_{ice} than compared to several types of pure mineral dust particles and thus are less ice nucleation efficient. However, the ice nucleation rate can only be evaluated if the effects of the available IN surface area and exposure time of particles to supersaturated conditions are accurately known as suggested by previous studies [*Kanji et al*., 2008; *Knopf and Alpert*, 2013]. It is very likely that inorganic sea salt or mineral dust particles intersecting with air masses that undergo photochemical processing involving volatile organic compounds obtain readily coatings of secondary organic material [*Hallquist et al*., 2009; *Jimenez et al*., 2009; *Laskin et al*., 2012]. This further emphasizes the importance of understanding the chemical and physical properties of the condensed phase organics, in particular at temperatures below the ice melting point.

Our findings that ambient organic dominated-particles cannot be ruled out as potential IN support previous reports [*Baustian et al*., 2012; *Hiranuma et al*., 2013; *Knopf et al*., 2010; *Wang et al*., 2012b]. Previous studies have shown that the condensed-phase organic material, which may be secondary in nature, is likely solid or highly viscous in nature at these low temperatures and for this reason can initiate ice nucleation [*Baustian et al*., 2013; *Murray et al*., 2010; *Wang et al*., 2012a; *Wilson et al*., 2012]. Since the physicochemical and morphological characteristics of identified IN are indistinguishable from the particles of the same major particle-type classes, particle composition alone may not result in accurate prediction of the onset of ice nucleation. Other potential parameters that govern ice nucleation rate and which may not be readily available in sufficient accuracy may include (i) the total particle surface area of the particle-type class that induced ice nucleation, (ii) the organic coating thickness in combination with the underlying morphological surface roughness, (iii) the oxidation degree of organic compounds, and (iv) the particle phase state and corresponding viscosity.

4. Conclusions

We introduced a novel analytical methodology that allows comprehensive microspectrosopic single-particle analyses to characterize an ambient particle population and individual ice-active particles. Based on the particles-on-substrate approach, this methodology employs a complementary analysis for ice nucleation and IN identification using optical microscopy coupled to a custom-built ice nucleation cell, CCSEM/EDX, and STXM/NEXAFS. We show that water uptake and ice nucleation experiments for temperatures as low as 200 K can be conducted for various substrates typically applied in single-particle microspectroscopy. The method allows the identification and characterization of single particles acting as IN. The benefits of this approach to advance our understanding of aerosol-cloud interactions, including ice formation, are manifold. Sample collection is simple and economic, necessitating solely an impactor and substrates [*Knopf et al*., 2010; *Wang et al*., 2012b]. Both, the particle population on a statistically significant level and the individual IN are characterized using a variety of state-of-the-art single-particle microspectroscopic analyses and chemical imaging. The application of particle samples allows us to probe water uptake, IMF, and DIN for the entire atmospheric temperature and RH range. This also allows us to probe the conditions before and after cloud initiation by evaluating the importance of aerosol-cloud cycles, since the identical particles can be repeatedly exposed to water uptake and ice nucleation. However, this precludes other important aspects of cloud evolution such as coalescence processes and multiphase chemistry. This can have important consequences for ice nucleation such as preactivation [*Knopf and Koop*, 2006], amorphous organic phase states [*Adler et al*., 2013; *Wang et al*., 2012a], chemical reactive surfaces, cloud condensation nuclei activation, and optical properties [*Adler et al*., 2013].

The presented approach was applied to characterize individual IN and the ambient particle population that were affected by biogenic and anthropogenic emissions collected in central California. Our results indicate that all particles are associated with organic coatings and are impacted by a marine source. Depletion of chlorine in the condensed phase was ubiquitous. The organic material is enriched in carboxylic functionalities, suggesting that it is oxidized and thus secondary in nature. Coarse mode particles are characterized as aged sea salt particles (depleted in chlorine) and fresh sea salt particles, both associated with organic material. Most abundant fine mode particles are Na-rich carbonaceous, secondary carbonaceous, and refractory carbonaceous in nature. Particle populations sampled at the T0 ground site did not include bare inorganic particles such as pure sea salt or mineral dust particles. It is very likely that inorganic sea salt or mineral dust particles acquire coatings of SOA material when intersecting with air masses rich in products from the photochemical processing of volatile organic compounds [*Hallquist et al*., 2009; *Jimenez et al*., 2009]. This further emphasizes the importance of understanding the chemical and physical properties of the condensed phase organics, in particular at temperatures below the ice melting point.

The identified IN in this study belong to major particle-type classes and induce ice formation through IMF mode for temperatures 226–247 K and DIN below 226 K, reflecting tropospherically relevant conditions. The ice nucleating particles are associated with organic materials and/or possess organic coatings and do not exhibit morphologically and compositionally distinctive features compared to other particles of the same particle-type class. It follows that particle composition and morphology do not allow a clear distinction between the ice nucleating and the non-ice nucleating particles within a specific particle-type class. Our findings support the notion that the IN are not always the exception within the particle population and as such do not necessarily represent "a needle in the haystack" challenge. However, it corroborates our previous findings based on statistical analysis that other parameters are also important. Factors such as particle abundance and total particle surface area [*Knopf et al*., 2010; *Wang et al*., 2012b] may govern the ice nucleation rate and thus the ice formation processes. It has been shown by us and others [e.g., *Kanji et al*., 2008; *Knopf and Alpert*, 2013] that ice nucleation depends on available particle surface area. Ice nucleation experiments on particle samples with different particle loadings acquired from the same ambient air mass will help to shed light on the parameters governing ice nucleation kinetics. Furthermore, ice nucleation is surface and time dependent and stochastic in nature [*Knopf and Alpert*, 2013; *Pruppacher and Klett*, 1997]. It can be anticipated that ice nucleation occurrence is statistically distributed on any of the particles present within the particular particle-type class. This can explain why the IN are not necessarily the largest particle within the particle-type class when compared to the surrounding non-ice nucleating particles. An important implication of our findings is that particle-type abundance, representing a uniform ice nucleating surface area, can also govern ice formation in an ambient particle population. In other words, knowledge of the freezing temperature and kinetics (efficiency) of a specific particle-type acting as IN is necessary but not sufficient to predict ice nucleation in the atmosphere. The particles' abundance and total available surface area in relation to other potentially ice nucleating particles should be considered in applying classical nucleation theory (CNT) as an ice nucleation parameterization including parameters such as the heterogeneous ice nucleation rate coefficient [*Pruppacher and Klett*, 1997]. This challenges the concept of IN as a measurable and defined number (e.g., IN per liter of air). We argue conceptually (based on CNT) that all particles in a population can act as IN given that their total surface area and ice nucleation efficiency combined are of significant influence for the ice nucleation rate. Laboratory ice nucleation experiments that apply particle samples composed of different efficient IN can help to resolve these issues in future studies. Atmospheric measurements should be accompanied by IN and particle population composition analysis. We believe that our results stimulate research in this direction which would yield improved parameterization approaches for ice nucleation in cloud models. Finally, our findings support the potential importance of globally ubiquitous organic particles to affect ice nucleation in the atmosphere with subsequent consequences for the hydrological cycle and climate.

Acknowledgments

The data for this paper are available upon request from the authors. Funding for sample collection during CARES study was provided by the Atmospheric Radiation Measurement Program sponsored by the U.S. Department of Energy (DOE), Office of Science, Office of Biological and Environmental Research (OBER), Climate and Environmental Sciences Division (CESD). Funding for the data analysis was provided by the U.S. DOE's Atmospheric System Research Program, OBER, CESD. B. Wang acknowledges the support of Laboratory Directed Research and Development funds of Pacific Northwest National Laboratory (PNNL). PNNL is operated by the U.S. DOE by Battelle Memorial Institute under contract DE-AC06-76RL0. The CCSEM/EDX particle analysis was performed in the Environmental Molecular Sciences Laboratory, a national scientific user facility sponsored by OBER at PNNL. The STXM/NEXAFS particle analysis was performed at beamlines 11.0.2 and 5.3.2 at the Advanced Light Source (ALS) at Lawrence Berkeley National Laboratory. The work at the ALS was supported by the Director, Office of Science, Office of Basic Energy Sciences, of the U.S. DOE under contract DE-AC02-05CH11231. We thank A.L.D. Kilcoyne and T. Tyliszczak for their assistance with the STXM experiments F. Jones is acknowledged for assisting in the ice nucleation experiments. J. Seong is acknowledged for the production of the movie file.

References

Adler, G., T. Koop, C. Haspel, I. Taraniuk, T. Moise, I. Koren, R. H. Heiblum, and Y. Rudich (2013), Formation of highly porous aerosol particles by atmospheric freeze-drying in ice clouds, *Proc. Natl. Acad. Sci. U.S.A.*, *110*(51), 20,414–20,419, doi:10.1073/pnas.1317209110.

Alpert, P. A., J. Y. Aller, and D. A. Knopf (2011), Initiation of the ice phase by marine biogenic surfaces in supersaturated gas and supercooled aqueous phases, *Phys. Chem. Chem. Phys.*, *13*(44), 19,882–19,894.

Baker, A., and T. Peter (2008), Small-scale cloud processes and climate, *Nat. Geosci.*, *451*(17), 299–300.

Baker, M. B. (1997), Cloud microphysics and climate, *Science*, *276*(5315), 1072–1078.

Baustian, K. J., D. J. Cziczo, M. E. Wise, K. A. Pratt, G. Kulkarni, A. G. Hallar, and M. A. Tolbert (2012), Importance of aerosol composition, mixing state, and morphology for heterogeneous ice nucleation: A combined field and laboratory approach, *J. Geophys. Res.*, *117*, D06217, doi:10.1029/2011JD016784.

Baustian, K. J., M. E. Wise, E. J. Jensen, G. P. Schill, M. A. Freedman, and M. A. Tolbert (2013), State transformations and ice nucleation in amorphous (semi-)solid organic aerosol, *Atmos. Chem. Phys.*, *13*, 5615–5628, doi:10.5194/acp-13-5615-2013.

Beichert, P., and B. J. Finlayson-Pitts (1996), Knudsen cell studies of the uptake of gaseous HNO_3 and other oxides of nitrogen on solid NaCl: The role of surface-adsorbed water, *J. Phys. Chem.*, *100*(37), 15,218–15,228, doi:10.1021/jp960925u.

Benzerara, K., T. H. Yoon, T. Tyliszczak, B. Constantz, A. M. Spormann, and G. E. Brown (2004), Scanning transmission X-ray microscopy study of microbial calcification, *Geobiology*, *2*(4), 249–259, doi:10.1111/j.1472-4677.2004.00039.x.

Cheng, Y. Z. (1995), Mean shift, mode seeking, and clustering, *IEEE Trans. Pattern Anal. Mach. Intell.*, *17*(8), 790–799.

Cziczo, D. J., K. D. Froyd, C. Hoose, E. J. Jensen, M. H. Diao, M. A. Zondlo, J. B. Smith, C. H. Twohy, and D. M. Murphy (2013), Clarifying the dominant sources and mechanisms of cirrus cloud formation, *Science*, *340*(6138), 1320–1324, doi:10.1126/science.1234145.

DeMott, P. J., D. J. Cziczo, A. J. Prenni, D. M. Murphy, S. M. Kreidenweis, D. S. Thomson, R. Borys, and D. C. Rogers (2003), Measurements of the concentration and composition of nuclei for cirrus formation, *Proc. Natl. Acad. Sci. U.S.A.*, *100*(25), 14,655–14,660, doi:10.1073/pnas.2532677100.

DeMott, P. J., A. J. Prenni, X. Liu, S. M. Kreidenweis, M. D. Petters, C. H. Twohy, M. S. Richardson, T. Eidhammer, and D. C. Rogers (2010), Predicting global atmospheric ice nuclei distributions and their impacts on climate, *Proc. Natl. Acad. Sci. U.S.A.*, *107*(25), 11,217–11,222, doi:10.1073/pnas.0910818107.

Fenter, F. F., F. Caloz, and M. J. Rossi (1994), Kinetics of nitric-acid uptake by salt, *J. Phys. Chem.*, *98*(39), 9801–9810, doi:10.1021/j100090a014.

Fenter, F. F., F. Caloz, and M. J. Rossi (1996), Heterogeneous kinetics of N_2O_5 uptake on salt, with a systematic study of the role of surface presentation (for N_2O_5 and HNO_3), *J. Phys. Chem.*, *100*(3), 1008–1019.

Fukunaga, K., and L. D. Hostetler (1975), Estimation of gradient of a density-function, with applications in pattern-recognition, *IEEE Trans. Inf. Theory*, *21*(1), 32–40, doi:10.1109/tit.1975.1055330.

Ghorai, S., and A. V. Tivanski (2010), Hygroscopic behavior of individual submicrometer particles studied by X-ray spectromicroscopy, *Anal. Chem.*, *82*(22), 9289–9298, doi:10.1021/ac101797k.

Ghorai, S., A. Laskin, and A. V. Tivanski (2011), Spectroscopic evidence of Keto-enol tautomerism in deliquesced malonic acid particles, *J. Phys. Chem. A*, *115*(17), 4373–4380, doi:10.1021/jp112360x.

Gilles, M. K., R. C. Moffet, and A. Laskin (2010), Spectro-microscopy of carbonaceous particulates, *Geochim. Cosmochim. Acta*, *74*(12), A332.

Hallquist, M., et al. (2009), The formation, properties and impact of secondary organic aerosol: Current and emerging issues, *Atmos. Chem. Phys.*, *9*(14), 5155–5236.

Heald, C. L., et al. (2011), Exploring the vertical profile of atmospheric organic aerosol: Comparing 17 aircraft field campaigns with a global model, *Atmos. Chem. Phys.*, *11*(24), 12,673–12,696, doi:10.5194/acp-11-12673-2011.

Hiranuma, N., S. D. Brooks, R. C. Moffet, A. Glen, A. Laskin, M. K. Gilles, P. Liu, A. M. Macdonald, J. W. Strapp, and G. M. McFarquhar (2013), Chemical characterization of individual particles and residuals of cloud droplets and ice crystals collected on board research aircraft in the ISDAC 2008 study, *J. Geophys. Res. Atmos.*, *118*, 6564–6579, doi:10.1002/jgrd.50484.

Hoose, C., and O. Möhler (2012), Heterogeneous ice nucleation on atmospheric aerosols: A review of results from laboratory experiments, *Atmos. Chem. Phys.*, *12*(20), 9817–9854, doi:10.5194/acp-12-9817-2012.

Hopkins, R. J., K. Lewis, Y. Desyaterik, Z. Wang, A. V. Tivanski, W. P. Arnott, A. Laskin, and M. K. Gilles (2007a), Correlations between optical, chemical and physical properties of biomass burn aerosols, *Geophys. Res. Lett.*, *34*, L18806, doi:10.1029/2007GL030502.

Hopkins, R. J., A. V. Tivanski, B. D. Marten, and M. K. Gilles (2007b), Chemical bonding and structure of black carbon reference materials and individual carbonaceous atmospheric aerosols, *J. Aerosol Sci.*, *38*(6), 573–591, doi:10.1016/j.jaerosci.2007.03.009.

Hopkins, R. J., Y. Desyaterik, A. V. Tivanski, R. A. Zaveri, C. M. Berkowitz, T. Tyliszczak, M. K. Gilles, and A. Laskin (2008), Chemical speciation of sulfur in marine cloud droplets and particles: Analysis of individual particles from marine boundary layer over the California current, *J. Geophys. Res.*, *113*, D04209, doi:10.1029/2007JD008954.

Jimenez, J. L., et al. (2009), Evolution of organic aerosols in the atmosphere, *Science*, *326*(5959), 1525–1529, doi:10.1126/science.1180353.

Kanji, Z. A., O. Florea, and J. P. D. Abbatt (2008), Ice formation via deposition nucleation on mineral dust and organics: Dependence of onset relative humidity on total particulate surface area, *Environ. Res. Lett.*, *3*(2), 025004, doi:10.1088/1748-9326/3/2/025004.

Kilcoyne, A. L. D., et al. (2003), Interferometer-controlled scanning transmission X-ray microscopes at the Advanced Light Source, *J. Synchrotron Radiat.*, *10*, 125–136.

Knopf, D. A., and P. A. Alpert (2013), Water activity based model of heterogeneous ice nucleation kinetics for freezing of water and aqueous solution droplets, *Faraday Discuss.*, *165*, 513–534, doi:10.1039/C3FD00035D.

Knopf, D. A., and T. Koop (2006), Heterogeneous nucleation of ice on surrogates of mineral dust, *J. Geophys. Res.*, *111*, D12201, doi:10.1029/2005JD006894.

Knopf, D. A., L. M. Cosman, P. Mousavi, S. Mokamati, and A. K. Bertram (2007), A novel flow reactor for studying reactions on liquid surfaces coated by organic monolayers: Methods, validation, and initial results, *J. Phys. Chem. A*, *111*(43), 11,021–11,032, doi:10.1021/Jp075724c.

Knopf, D. A., B. Wang, A. Laskin, R. C. Moffet, and M. K. Gilles (2010), Heterogeneous nucleation of ice on anthropogenic organic particles collected in Mexico City, *Geophys. Res. Lett.*, *37*, L11803, doi:10.1029/2010GL043362.

Knopf, D. A., P. A. Alpert, B. Wang, and J. Y. Aller (2011), Stimulation of ice nucleation by marine diatoms, *Nat. Geosci.*, *4*(2), 88–90, doi:10.1038/ngeo1037.

Koop, T., B. P. Luo, A. Tsias, and T. Peter (2000a), Water activity as the determinant for homogeneous ice nucleation in aqueous solutions, *Nature*, *406*(6796), 611–614, doi:10.1038/35020537.

Koop, T., A. Kapilashrami, L. T. Molina, and M. J. Molina (2000b), Phase transitions of sea-salt/water mixtures at low temperatures: Implications for ozone chemistry in the polar marine boundary layer, *J. Geophys. Res.*, *105*(D21), 26,393–26,402, doi:10.1029/2000JD900413.

Koop, T., J. Bookhold, M. Shiraiwa, and U. Pöschl (2011), Glass transition and phase state of organic compounds: Dependency on molecular properties and implications for secondary organic aerosols in the atmosphere, *Phys. Chem. Chem. Phys.*, *13*(43), 19,238–19,255, doi:10.1039/c1cp22617g.

Laskin, A., M. J. Iedema, and J. P. Cowin (2003), Time-resolved aerosol collector for CCSEM/EDX single-particle analysis, *Aerosol Sci. Technol.*, *37*(3), 246–260.

Laskin, A., J. P. Cowin, and M. J. Iedema (2006), Analysis of individual environmental particles using modern methods of electron microscopy and X-ray microanalysis, *J. Electron Spectrosc. Relat. Phenom.*, *150*(2–3), 260–274, doi:10.1016/j.elspec.2005.06.008.

Laskin, A., R. C. Moffet, M. K. Gilles, J. D. Fast, R. A. Zaveri, B. B. Wang, P. Nigge, and J. Shutthanandan (2012), Tropospheric chemistry of internally mixed sea salt and organic particles: Surprising reactivity of NaCl with weak organic acids, *J. Geophys. Res.*, *117*, D15302, doi:10.1029/2012JD017743.

Liu, Y., Z. W. Yang, Y. Desyaterik, P. L. Gassman, H. Wang, A. Laskin, S. J. Kim, and J. Han (2008), Hygroscopic behavior of substrate-deposited particles studied by micro-FT-IR spectroscopy and complementary methods of particle analysis (vol 80, pg 633, 2008), *Anal. Chem.*, *80*(18), 7179, doi:10.1021/Ac801397q.

Michelsen, H. A., A. V. Tivanski, M. K. Gilles, L. H. van Poppel, M. A. Dansson, and P. R. Buseck (2007), Particle formation from pulsed laser irradiation of soot aggregates studied with a scanning mobility particle sizer, a transmission electron microscope, and a scanning transmission X-ray microscope, *Appl. Opt.*, *46*(6), 959–977.

Moffet, R. C., et al. (2008), Characterization of aerosols containing Zn, Pb, and Cl from an industrial region of Mexico City, *Environ. Sci. Technol.*, *42*(19), 7091–7097, doi:10.1021/Es7030483.

Moffet, R. C., T. Henn, A. Laskin, and M. K. Gilles (2010a), Automated chemical analysis of internally mixed aerosol particles using X-ray spectromicroscopy at the carbon K-edge, *Anal. Chem.*, *82*(19), 7906–7914.

Moffet, R. C., A. V. Tivanski, and M. K. Gilles (2010b), Scanning X-ray transmission microscopy: Applications in atmospheric aerosol research, in *Fundamentals and Applications in Aerosol Spectroscopy*, edited by R. Signorell and J. P. Reid, pp. 419–462, Taylor and Francis Books, Inc., Boca Raton, Fla.

Moffet, R. C., T. C. Rodel, S. T. Kelly, X. Y. Yu, G. T. Carroll, J. Fast, R. A. Zaveri, A. Laskin, and M. K. Gilles (2013), Spectro-microscopic measurements of carbonaceous aerosol aging in Central California, *Atmos. Chem. Phys.*, *13*(20), 10,445–10,459, doi:10.5194/acp-13-10445-2013.

Murphy, D. M., and T. Koop (2005), Review of the vapour pressures of ice and supercooled water for atmospheric applications, *Q. J. R. Meteorol. Soc.*, *131*(608), 1539–1565, doi:10.1256/Qj.04.94.

Murray, B. J., et al. (2010), Heterogeneous nucleation of ice particles on glassy aerosols under cirrus conditions, *Nat. Geosci.*, *3*(4), 233–237, doi:10.1038/ngeo817.

Murray, B. J., D. O'Sullivan, J. D. Atkinson, and M. E. Webb (2012), Ice nucleation by particles immersed in supercooled cloud droplets, *Chem. Soc. Rev.*, *41*(19), 6519–6554, doi:10.1039/c2cs35200a.

Pruppacher, H. R., and J. D. Klett (1997), *Microphysics of Clouds and Precipitation*, Kluwer Acad., Dordrecht.

Rieger, D., F. J. Himpsel, U. O. Karlsson, F. R. McFeely, J. F. Morar, and J. A. Yarmoff (1986), Electronic-structure of the CaF_2/Si(111) interface, *Phys. Rev. B*, *34*(10), 7295–7306, doi:10.1103/PhysRevB.34.7295.

Seinfeld, J. H., and S. N. Pandis (1998), *Atmospheric Chemistry and Physics*, John Wiley, New York.

Selim, S. Z., and M. A. Ismail (1984), K-means-type algorithms - A generalized convergence theorem and characterization of local optimality, *IEEE Trans. Pattern Anal. Mach. Intell.*, *6*(1), 81–87.

Takahama, S., S. Gilardoni, L. M. Russell, and A. L. D. Kilcoyne (2007), Classification of multiple types of organic carbon composition in atmospheric particles by scanning transmission X-ray microscopy analysis, *Atmos. Environ.*, *41*(40), 9435–9451, doi:10.1016/j.atmosenv.2007.08.051.

Thompson, S. K. (1987), Sample-size for estimating multinomial proportions, *Am. Stat.*, *41*(1), 42–46, doi:10.2307/2684318.

Thornton, J. A., et al. (2010), A large atomic chlorine source inferred from mid-continental reactive nitrogen chemistry, *Nature*, *464*(7286), 271–274, doi:10.1038/nature08905.

Tivanski, A. V., R. J. Hopkins, T. Tyliszczak, and M. K. Gilles (2007), Oxygenated interface on biomass burn tar balls determined by single particle scanning transmission X-ray microscopy, *J. Phys. Chem. A*, *111*(25), 5448–5458, doi:10.1021/jp070155u.

Wang, B. B., and D. A. Knopf (2011), Heterogeneous ice nucleation on particles composed of humic-like substances impacted by O_3, *J. Geophys. Res.*, *116*, D03205, doi:10.1029/2010JD014964.

Wang, B. B., A. T. Lambe, P. Massoli, T. B. Onasch, P. Davidovits, D. R. Worsnop, and D. A. Knopf (2012a), The deposition ice nucleation and immersion freezing potential of amorphous secondary organic aerosol: Pathways for ice and mixed-phase cloud formation, *J. Geophys. Res.*, *117*, D16209, doi:10.1029/2012JD018063.

Wang, B. B., A. Laskin, T. Roedel, M. K. Gilles, R. C. Moffet, A. V. Tivanski, and D. A. Knopf (2012b), Heterogeneous ice nucleation and water uptake by field-collected atmospheric particles below 273 K, *J. Geophys. Res.*, *117*, D00V19, doi:10.1029/2012JD017446.

Wilson, T. W., et al. (2012), Glassy aerosols with a range of compositions nucleate ice heterogeneously at cirrus temperatures, *Atmos. Chem. Phys.*, *12*(18), 8611–8632, doi:10.5194/acp-12-8611-2012.

Wise, M. E., E. J. Freney, C. A. Tyree, J. O. Allen, S. T. Martin, L. M. Russell, and P. R. Buseck (2009), Hygroscopic behavior and liquid-layer composition of aerosol particles generated from natural and artificial seawater, *J. Geophys. Res.*, *114*, D03201, doi:10.1029/2008JD010449.

Wittmaack, K. (2005), Brochosomes produced by leafhoppers-a widely unknown, yet highly abundant species of bioaerosols in ambient air, *Atmos. Environ.*, *39*(6), 1173–1180, doi:10.1016/j.atmosenv.2004.11.003.

Zaveri, R. A., et al. (2012), Overview of the 2010 Carbonaceous Aerosols and Radiative Effects Study (CARES), *Atmos. Chem. Phys.*, *12*(16), 7647–7687, doi:10.5194/acp-12-7647-2012.

Zhang, Q., et al. (2007), Ubiquity and dominance of oxygenated species in organic aerosols in anthropogenically-influenced Northern Hemisphere midlatitudes, *Geophys. Res. Lett.*, *34*, L13801, doi:10.1029/2007GL029979.